Method for Simulating Dose Reduction in Digital Breast Tomosynthesis

Lucas R. Borges, Igor Guerrero, Predrag R. Bakic, Alessandro Foi, Andrew D. A. Maidment, and Marcelo A. C. Vieira

***Abstract*—This work proposes a new method of simulating dose reduction in digital breast tomosynthesis (DBT), starting from a clinical image acquired with a standard radiation dose. It considers both signal-dependent quantum and signal-independent electronic noise. Furthermore, the method accounts for pixel crosstalk, which causes the noise to be frequency-dependent, thus increasing the simulation accuracy. For an objective assessment, simulated and real images were compared in terms of noise standard deviation, signal-to-noise ratio (SNR) and normalized noise power spectrum (NNPS). A two-alternative forced-choice (2-AFC) study investigated the similarity between the noise strength of low-dose simulated and real images. Six experienced medical physics specialists participated on the study, with a total of 2,160 readings. Objective assessment showed no relevant trends with the simulated noise. The relative error in the standard deviation of the simulated noise was less than 2% for every projection angle. The relative error of the SNR was less than 1.5%, and the NNPS of the simulated images had errors less than 2.5%. The 2-AFC human observer experiment yielded no statistically significant difference (p=0.84) in the perceived noise strength between simulated and real images. Furthermore, the observer study also allowed the estimation of a dose difference at which the observer perceived a just-noticeable difference (JND) in noise levels. The estimated JND value indicated that a change of 17% in the current-time product was sufficient to cause a noticeable difference in noise levels. The observed high accuracy, along with the flexible calibration, make this method an attractive tool for clinical image-based simulations of dose reduction.**

***Index Terms*—Electronic noise, digital breast tomosynthesis, dose reduction, quantum noise.**

I. Introduction

DIGITAL breast tomosynthesis (DBT) is rapidly emerging as a major clinical tool for breast cancer screening. In DBT, a set of radiographic projections is acquired within a limited angular range around the breast. The projections are then reconstructed into a 3D volume made up of tomographic slices of the breast. The 3D visualization of the breast anatomy reduces tissue overlap if compared to conventional mammography, thus increasing the sensitivity and specificity of cancer detection [1]–[3].

This work was supported by the São Paulo Research Foundation (FAPESP grant no. 2016/25750-0), by the Brazilian Foundation for the Coordination of Improvement of Higher Education Personnel (CAPES grant no. 88881.030443/2013-01) and by the Academy of Finland (project no. 252547).

L.R. Borges, I. Guerrero and M.A.C. Vieira are with the University of São Paulo, Brazil (e-mail: lucas.rodrigues.borges@usp.br, igor.guerrero@usp.br, mvieira@sc.usp.br); A. Foi is with Tampere University of Technology, Finland (e-mail: alessandro.foi@tut.fi); P.R. Bakic and A.D.A. Maidment are with the University of Pennsylvania (e-mail: predrag.bakic@uphs.upenn.edu, andrew.maidment@uphs.upenn.edu).

As DBT is still being developed, the optimization of radiation dose is an open issue [4], [5]. The International Basic Safety Standards for Protection against Ionizing Radiation and for the Safety of Radiation Sources defines that diagnostic exposures of patients must "be the minimum necessary to achieve the required diagnostic objective" [6]. The literature presents a variety of approaches to achieve dose savings while maintaining the desired image quality. Some examples are the optimization of acquisition protocols [7], [8], the application of post-processing filters to low-dose projections [9], the development of iterative reconstruction methods [10], [11].

To validate these studies and enforce the minimum dose requirement, it is desirable to have a set of clinical images acquired from the same patient at different radiation doses. However, the availability of such images is extremely limited, since it requires the repeated exposure of patients to x-rays.

One common approach to overcome this limitation is to perform simulations of dose reduction through the injection of quantum noise in clinical images acquired with the standard radiation dose [12]–[14]. In fact, many of the studies regarding the optimization of radiation dose for radiographic imaging systems were conducted using simulated images [15], [16].

X-ray imaging commonly involves signal-dependent noise models where the variance of the noise is expressed as a function of the noise-free signal. Since the noise-free signal is not usually available, some methods simulate signal-dependent noise by approximating, in the definition of the variance, the noise-free signal by the noisy one [12]–[14]. This approximation can be rather coarse, mainly at a reduced count-rate regime [17].

In previous work, we proposed a method of simulating dose reduction in full-field digital mammography (FFDM) images, based on noise injection in a variance-stabilized range [17], [18]. It has the advantage that no previous knowledge of the noise-free signal is needed, avoiding errors due to approximation. However, although it is a precise method for the simulation of 2D digital mammography, it has some constraints that limited the performance of the method to digital breast tomosynthesis (DBT) images [19]: the noise was modeled exclusively as white Poisson noise, that is, it does not consider the spatial correlation between pixels of acquisition system (detector crosstalk) and also does not consider the electronic noise of the equipment. Moreover, the method needs two sets of calibration images: one with the same radiographic factors of the original clinical image (standard dose) and other with the radiographic factors of the simulated low-dose image, which is a challenge for clinical applicability.

Because individual DBT projections are acquired at substantially lower radiation levels, the overall signal at each projection is lower. In a reduced count-rate regime, the additive electronic noise plays an important role and has to be considered in the noise model [20], [21]. Furthermore, approximations of the noise-free signal, commonly applied for the simulation of signal-dependent noise, become coarse at lower counting regimes and thus limits the performance of the simulation methods.

Thus, this work proposes a new method of simulating dose reduction in DBT. It considers both quantum and electronic noise sources, the noise spatial correlation, and eliminates approximations of the noise-free signal. The method also has high clinical practicality, since the number of calibration images is reduced. Moreover, we present an extensive validation of the algorithm through objective measurements and human observer experiments. Although the present work focuses on the validation of the simulation method to DBT images, the algorithm can be explored in other imaging modalities that present similar noise properties.

II. Preliminaries

A. DBT imaging system

In a DBT system, the breast is compressed and kept stationary while the x-ray tube moves around it in a limited angular range. During the movement, a series of raw projections are acquired. The raw projections go through a reconstruction process to generate slices parallel to the detector, known as reconstructed slices. The slices are then transmitted to a diagnostic workstation to be assessed by a radiologist [20].

The proposed simulation method performs mathematical operations on the raw projections, acquired with a standard radiation dose, to simulate lower-dose acquisitions. After the simulation is performed, the simulated projections must be reconstructed to generate lower-dose reconstructed slices.

B. Problem formulation

Let $z_{\text{in}}(i,j)$ be observed pixels at positions (i,j) of a DBT raw projection image. We model the input variable z_{in} as

$$z_{\text{in}}(i,j) = y(i,j) + \tau + s(y(i,j))\,\xi(i,j)\,, \tag{1}$$

where $y > 0$ is the (unknown) noise-free signal, proportional to the energy of the x-rays reaching the detector, $\tau > 0$ is the signal intensity offset, ξ is signal-independent random noise with zero mean and unit variance, and s is a function of y that defines the standard deviation of the overall noise. At each pixel, the expectation and variance of z_{in} are modeled as

$$\mathrm{E}\{z_{\text{in}}(i,j)|y(i,j)\} = y(i,j) + \tau\,, \tag{2}$$

$$s^2(y(i,j)) = \mathrm{var}\{z_{\text{in}}(i,j)|y(i,j)\} = y(i,j)\,\lambda_{\text{in}}(i,j) + \sigma_{\text{E}}^2\,, \tag{3}$$

where λ_{in} is the linear coefficient of the noise variance function, which can be attributed to the quantum efficiency and gain in the image formation, and σ_{E}^2 is the variance of the signal-independent portion of the noise. The above model (2)-(3) can also be used, in practice, in the presence of spatial correlation caused by pixel crosstalk at the detector, as discussed in Appendix A. The ratio between y and $s(y)$ gives the pixelwise signal-to-noise ratio (SNR) of z_{in}. For a given current and kVp, shorter exposure time means lower radiation dose, hence smaller y and consequently lower SNR.

Our goal is to obtain from z_{in} a new set of noisier observations z_{out} that simulate a lower-dose acquisition and fulfill the following conditions:

$$\mathrm{E}\{z_{\text{out}}(i,j)|y(i,j)\} = \gamma y(i,j) + \tau, \tag{4}$$

$$\mathrm{var}\{z_{\text{out}}(i,j)|y(i,j)\} = \gamma y(i,j)\,\lambda_{\text{in}}(i,j) + \sigma_{\text{E}}^2, \tag{5}$$

where $0 < \gamma < 1$ is the dose reduction factor that we wish to simulate.

III. Method

The proposed method consists of five steps: linearization, injection of quantum noise, signal scaling, injection of electronic noise, and injection of signal offset. The method requires a set of raw clinical DBT projections and a set of raw uniform projections acquired with the same radiographic factors as the clinical DBT, which henceforth are named calibration projections. The five-step algorithm is applied to each raw projection of the clinical DBT, using the respective raw projection of the calibration image. The calibration image is required for the estimation of parameters. Fig. 1 shows an overview of the complete pipeline.

A. Estimation of parameters

For the correct application of the dose-reduction simulation pipeline, it is important to correctly estimate the noise and signal parameters τ, σ_{E}^2, and λ_{in}.

1) Pixel offset τ: The National Health Service Breast Screening Program (NHSBSP) [22] has developed a practical method of calculating the pixel offset, which we applied in this work. Another alternative method of estimating pixel offset is by acquiring a dark-field image [23].

2) Variance of the electronic noise σ_E^2: The variance σ_{E}^2 can be estimated using noise parameter estimation algorithms [24]–[26]. For this purpose, we use software [25], available for download [27]. The software can estimate the standard deviation of the additive portion of signal-dependent noise provided that the pixel gain is constant through the field. To enable this, we selected a rectangular region of interest (ROI) with a short span along the anterior-posterior direction and much longer span along the orthogonal direction, located near the chest wall. Using this elongated ROI, we take advantage of the fact that the pixel gain varies more slowly in the orthogonal direction than in the anterior-posterior direction, due to the flat-field correction commonly used in commercial DBT systems. The estimation of σ_{E}^2 is performed using raw projections from the input DBT clinical images.

3) Linear coefficient λ_{in} of the noise variance function: The ideal way of obtaining λ_{in} would be by accessing the calibration data of the clinical unit used to acquire the DBT projections. However, this information is not easily available and thus λ_{in} has to be estimated from the acquired images. We estimate λ_{in} using the calibration image given as input, acquired at the same radiographic factor as the original image.

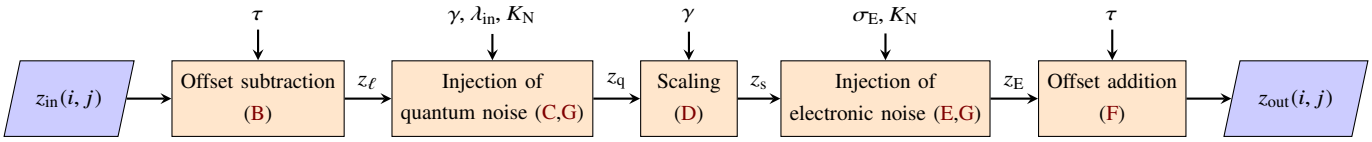

Fig. 1. Overview of the proposed dose-reduction simulation pipeline. Reconstruction methods can be applied to z_{out}, generating lower-dose tomosynthesis slices. The capital letters in parentheses refer to the corresponding subsections within Section III.

The estimation can be performed using a simple derivation of the standard deviation model presented in (2) and (3):

$$\lambda_{\text{in}}(i,j) = \frac{\hat{\sigma}^2(i,j) - \sigma_{\text{E}}^2}{\hat{\mu}(i,j) - \tau}, \tag{6}$$

where $\hat{\mu}(i,j)$ and $\hat{\sigma}^2(i,j)$ are, respectively, the local mean and local variance estimated from the calibration image. Values of τ, σ_{E}^2, and λ_{in} for the system used in our experimental results are given in Section IV.

B. Offset subtraction

To scale the intensity of the clinical image correctly, the method requires a linear relationship between the expectation of the observed signal z_{in} and the underlying signal y. Thus, we define the linearized signal $z_\ell(i,j)$ as

$$z_\ell(i,j) = z_{\text{in}}(i,j) - \tau. \tag{7}$$

C. Injection of quantum noise

In previous work, we proposed an operator capable of injecting signal-dependent quantum noise through a variance-stabilizing transformation (VST) [17], [18], [28]. We have implemented the method to simulate dose reduction in FFDM images [18], and optimized the operator to maintain high performance even for applications with limited count rate [17].

In the current work we propose the injection of quantum noise through a nonlinear operator Φ. In DBT images, the electronic portion of the noise represents a relevant part of the image degradation, thus the operator must be adequate for signal-dependent noise models with affine variance like (3). The operator changes the variance of the combination of input noise and of the injected noise so as to yield the desired signal-dependent quantum noise for the reduced-dose output. It does not require previous knowledge of the shape of the distribution ξ or of the noise-free signal $y(i,j)$, therefore decreasing bias due to approximations, as shown in [17]. Considering the linearized DBT signal $z_\ell(i,j)$, we define the operator Φ as

$$z_{\text{q}}(i,j) = \Phi\left[z_\ell(i,j)\right] = \frac{\lambda_{\text{in}}(i,j)}{4}\left(x^2(i,j) - \frac{\sigma_{\text{A}}^2}{2}\right), \tag{8}$$

where $\sigma_{\text{A}} = \sqrt{(1/\gamma) - 1}$ and $x(i,j)$ is obtained by applying a root transformation to $z_\ell(i,j)$, followed by addition of signal-independent Gaussian noise with variance σ_{A}^2:

$$x(i,j) = 2\sqrt{\frac{z_\ell(i,j)}{\lambda_{\text{in}}(i,j)} - \frac{\sigma_{\text{A}}^2}{8}} + \sigma_{\text{A}}\eta(i,j), \tag{9}$$

η being Gaussian noise with zero mean and unit variance, $\eta(i,j) \sim \mathcal{N}(0,1)$. The mean and variance of z_{q} are

$$\text{E}\{z_{\text{q}}(i,j)\,|y(i,j)\,\} = y(i,j)\,, \tag{10}$$

$$\text{var}\{z_{\text{q}}(i,j)\,|y(i,j)\,\} = \frac{y(i,j)\,\lambda_{\text{in}}(i,j)}{\gamma} + \sigma_{\text{E}}^2. \tag{11}$$

The variable $z_{\text{q}}(i,j)$, modulo multiplication by the dose reduction factor γ, has quantum noise with the target linear scaling λ_{out}. In Appendix B we provide a method to obtain the operator Φ and discuss its properties.

D. Scaling

The next step is to scale the overall signal of the DBT image. Because the input signal was linearized previously, this can be done by multiplying $z_{\text{q}}(i,j)$ by the dose reduction factor γ:

$$z_{\text{s}}(i,j) = \gamma z_{\text{q}}(i,j)\,. \tag{12}$$

Both the mean and variance of $z_{\text{s}}(i,j)$ match those in (4)-(5), but only limited to the terms linear on $y(i,j)$. Hence, further adjustments are necessary to account for the electronic additive noise and offset.

E. Injection of electronic noise

After the above scaling, the variance of the additive electronic noise is also scaled to lower values. Thus, to fulfill (5), extra signal-independent noise is added to achieve the variance σ_{E}^2 of the electronic noise found in a clinical acquisition:

$$z_{\text{E}}(i,j) = z_{\text{s}}(i,j) + \sigma_\nu \nu(i,j)\,, \tag{13}$$

where $\sigma_\nu = \sqrt{\sigma_{\text{E}}^2\,(1-\gamma^2)}$ and ν is zero-mean Gaussian noise with unit variance, $\nu(i,j) \sim \mathcal{N}(0,1)$. The variance of z_{E} is

$$\text{var}\{z_{\text{E}}(i,j)\,|y(i,j)\,\} = \gamma y(i,j)\,\lambda_{\text{in}}(i,j) + \sigma_{\text{E}}^2\,. \tag{14}$$

The variable $z_{\text{E}}(i,j)$ achieves the target signal-dependent variance (5). Note that both noise injection steps (8) and (13) are pointwise and therefore it is irrelevant towards (4) and (5) whether the random variables z_ℓ or x are spatially uncorrelated or not. In fact, in our work, the injected noises η and ν are both spatially correlated to simulate the detector crosstalk, as detailed in Section III.G. The final adjustment addresses the target expectation.

F. Offset addition

Finally, the offset τ subtracted from the signal in the linearization step is added back to the signal:

$$z_{\text{out}}(i,j) = z_{\text{E}}(i,j) + \tau\,. \tag{15}$$

In this way, we attain both (4) and (5) exactly.

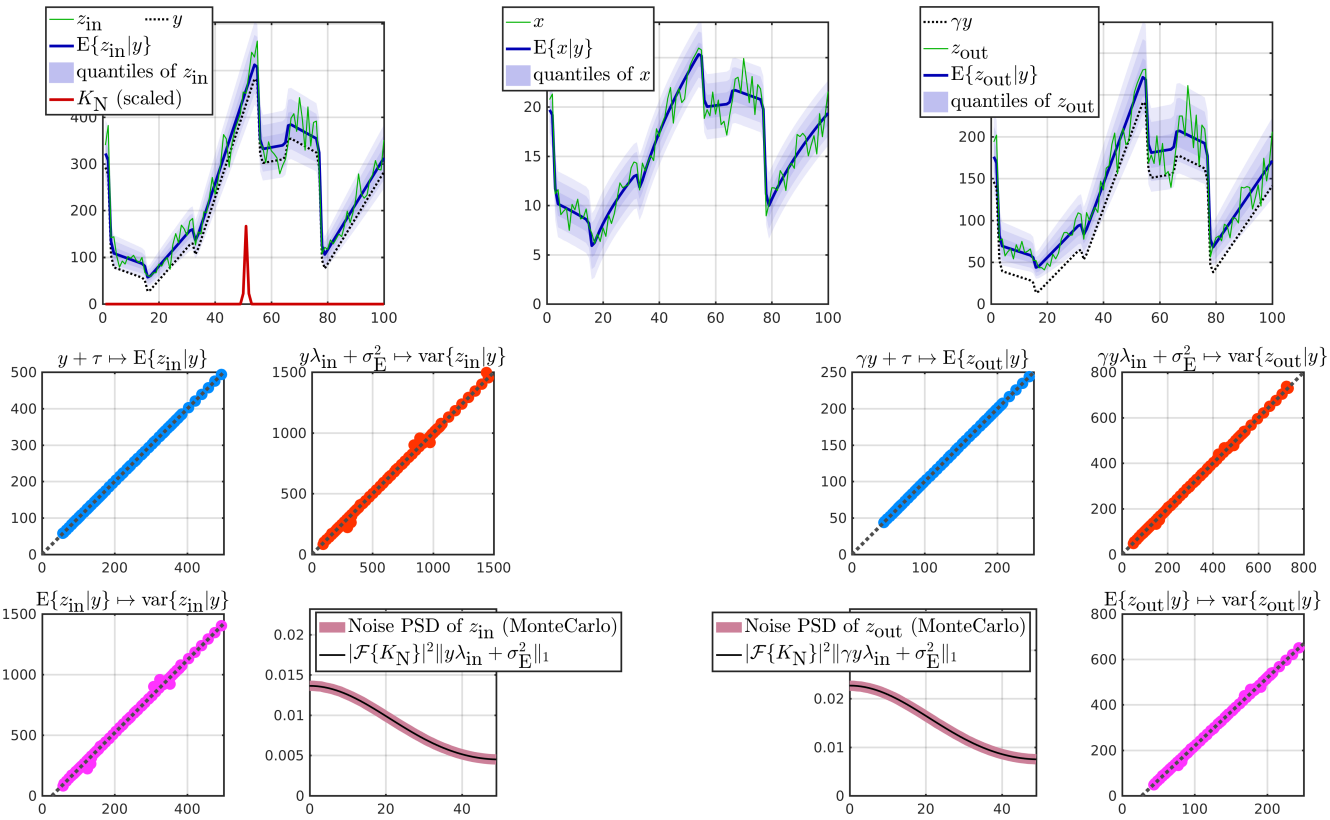

Fig. 2. Exemplary simulation using a 1D piecewise affine signal. The top row shows the input signal z_{in} (1) with parameters $\lambda_{\text{in}} = 3$, $\sigma_{\text{E}} = 3$, $\tau = 30$ (left), the transformed signal x used internally by the operator Φ (9) (center) and the output signal z_{out} obtained at the end of the proposed pipeline for a dose reduction factor $\gamma = 0.5$ (right). The kernel K_{N} is Gaussian with standard deviation 0.5. The four plots to the left show the expectation, variance and noise power spectrum for the input z_{in} computed from a MonteCarlo experiment with 10^6 realizations and compare these statistics with the analytical expressions in (2), (3) and (17). The four plots to the right visualize the same statistics for the output z_{out} and compare them with (4), (5), and (18), demonstrating accurate achievement of the design goals.

G. Detector crosstalk

In this work, we also consider the detector crosstalk, which causes the noise spectrum to be frequency-dependent (i.e. colored noise). This phenomenon is modeled through the power spectral density (PSD) Ψ of the noise. In practice, we compute Ψ from the calibration image through Fourier measurements over a running window as

$$\Psi = \frac{1}{M}\sum_{k=1}^{M} |\mathcal{F}\{I_{(i_k,j_k)} - S_{(i_k,j_k)}\}|^2, \tag{16}$$

where $I_{(i_k,j_k)}$ and $S_{(i_k,j_k)}$ are, respectively, the noisy calibration image and the local estimate of the noise-free image, over a window centered at (i_k, j_k). The window selection and estimation S are detailed in Section IV. As we work with a single calibration image, we make a simplifying assumption that a unique PSD describes the correlation within the quantum noise as well as the correlation within electronic noise; we discuss this assumption further in Section VI.

Based on (3) and (5) (see also Appendix A), the noise PSD for z_{in} and z_{out} can be modeled as

$$\Psi_{z_{\text{in}}} = |\mathcal{F}\{K_{\text{N}}\}|^2\|y\lambda_{\text{in}} + \sigma_{\text{E}}^2\|_1\,, \tag{17}$$

$$\Psi_{z_{\text{out}}} = |\mathcal{F}\{K_{\text{N}}\}|^2\|\gamma y\lambda_{\text{in}} + \sigma_{\text{E}}^2\|_1\,, \tag{18}$$

where K_{N} is a convolution kernel that relates to Ψ as

$$K_{\text{N}} = K\|K\|_2^{-1}, \qquad K = \mathcal{F}^{-1}\left\{\sqrt{\Psi}\right\}. \tag{19}$$

Hence, given a standard-dose image z_{in} subject to (2), (3) and (17), our goal is to simulate a reduced dose-image z_{out} that satisfies (4), (5), and (18). To this end, we generate correlated noises η (9) and ν (13) by convolving independent and identically distributed (IID) standard Gaussian white noises ω_η and ω_ν against K_{N}:

$$\eta = K_{\text{N}} * \omega_\eta\,, \qquad \nu = K_{\text{N}} * \omega_\nu\,, \tag{20}$$

where $*$ denotes the convolution operation. Because K_{N} has unit ℓ^2 norm, both η and ν inherit the unit pointwise variance of ω_η and ω_ν.

Note that, being nonlinear, the operator Φ (8) may distort the correlation model of η when transforming the injected noise into quantum noise. However, in practice such distortions are not significant for the conditions described in this work.

H. Exemplary simulation

Before demonstrating the proposed approach on real DBT imagery, we illustrate it over a simulated 1D signal, as shown

in Fig. 2. This serves both as a validation of the procedure and as more direct visualization. Note that the shape of the quantile regions visualizes the signal-dependent variance of the signal z_{in} and z_{out}, whereas in x it is practically homoskedastic.

IV. Experimental setup

All images used in this work were acquired using a Selenia Dimensions (Hologic, Bedford, MA) DBT unit at the Hospital of the University of Pennsylvania. The system is equipped with an amorphous selenium (a-Se) detector layer that has a thickness of 200 μm and pixel pitch of 140 μm. A total of 15 projections were acquired within an angular range of 15°.

The pixel offset τ was calculated using the protocol described by the NHSBPS [22], and a collection of central projections of uniform images acquired at four current-time products (60, 52, 42, and 30 mAs). The estimated τ for our experiments was 42.

The standard deviation σ_{E} of the electronic noise was estimated from an exposure of the anthropomorphic breast phantom in automatic exposure control mode (AEC), 31 kV_p, tungsten target, aluminum filter and 60 mAs, using a 7 mm × 105 mm ROI positioned close to the chest wall of and the methodology [25]. The estimated σ_{E} was 2.31.

Previous work on the same machine model found similar values of τ and σ_{E} [29]. Note that we used the same estimates of τ and σ_{E} for every experiment, as they do not change significantly over the dose levels considered in our experiments.

The parameters K_{N} and λ_{in} may change with the system calibration, and were thus estimated from calibration images acquired at the same radiographic factor as the input DBT used in the individual experiments; this is further specified in Sections IV.A and IV.B. Moreover, each projection angle requires a separate estimate of K_{N} and λ_{in}.

The convolution kernel K_{N} was estimated using a 64 × 64 running window with 50% overlap taken from the calibration projections according to (16) and (19). For the experiments, S is given as the mean value of I over the window. Fig. 3a shows one example of the estimated normalized kernel K_{N}.

The scaling factor λ_{in} was estimated using a 63 × 63 fully overlapping sliding window taken from the calibration images, and the relation defined by (6). Fig. 3b shows one example of the estimated map of local λ_{in} values at the central projection. Noteworthy, the parameter presented more relevant changes on the anterior-posterior (A-P) than on the orthogonal direction, as previously described in Section III.

A. Objective analysis

To assess the performance of the proposed method, objective metrics were calculated from uniform images. The uniform background allows for easy estimation of the signal and noise features.

The set of uniform images was obtained using a 4 cm poly methyl methacrylate (PMMA) block commonly used for flat-fielding the mammography system. The radiographic factors were manually set to 31 kV_p, tungsten target and aluminum filter and the current-time product was reduced

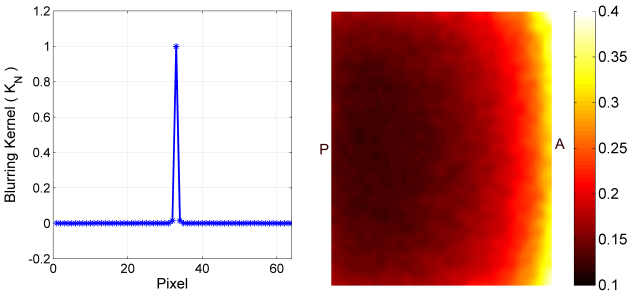

Fig. 3. Example of estimated parameters from the central projection of a calibration image acquired with 60 mAs, and 31 kV_p. (a) Convolution kernel K_{N} (standard deviation 0.3). (b) Linear coefficient λ_{in} of the signal-dependent noise. Labels: P (posterior), A (anterior).

from 60 mAs to 52 mAs, 42 mAs and 30 mAs, to achieve reduced dose images. Two acquisitions were performed at each configuration, resulting in eight sets of 15 projections each.

The fidelity of the simulated images was investigated by comparing simulated images and real images acquired at the simulated radiation level. The comparison was done in terms of standard deviation, SNR, and normalized noise power spectrum (NNPS). First, the local standard deviation of the noise was estimated inside a fully overlapping 63 × 63 sliding window. The average relative error E_σ was calculated as

$$E_\sigma = \frac{100\%}{M} \sum_{k=1}^{M} \frac{\sigma_{\text{R}}(i_k, j_k) - \sigma_{\text{S}}(i_k, j_k)}{\sigma_{\text{R}}(i_k, j_k)}, \tag{21}$$

where $\sigma_{\text{R}}(i_k, j_k)$ and $\sigma_{\text{S}}(i_k, j_k)$ are the local noise standard deviations of the real and simulated images, respectively, estimated from a window centered at the pixel (i_k, j_k), and M is the total number of windows.

Next, the SNR was estimated as the ratio between the signal mean and local standard deviation of the noise using the same window configuration mentioned above. The average relative error was calculated using the same approach as (21).

The last objective analysis used the NNPS [23], [30]. The NNPS was calculated for each projection using non-overlapping 64×64 pixels windows, taken from the central portion of the uniform images. The reported NNPS is the average of the spectra calculated for each window. The average relative error was calculated using (21).

Dependency on the calibration: Additional experiments were conducted to investigate the influence of the calibration images on the simulation performance. Ideally, the calibration image should be acquired with the same radiographic factors as the clinical image given as input, and using a PMMA block with attenuation similar to the breast, to enable the assumptions of the noise and signal models (1). Obtaining a wide range of calibration images can be clinically challenging, so we investigated the impact of using non-ideal calibration images as input for the simulation method.

The experiment was set as follows: uniform images were acquired using a 4 cm PMMA block at 31 kV_p, with 60 mAs and 30 mAs. The proposed simulation method was applied

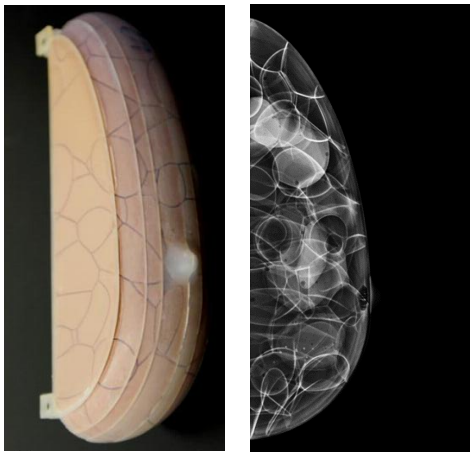

(a) (b)

Fig. 4. Anthropomorphic breast phantom used for the human observer studies. (a) Photograph of the phantom. (b) Sample of the central slice.

to the 60 mAs image, simulating 30 mAs images, using a range of calibration images as input. The calibration images were acquired using combinations of 2 cm, 4 cm, and 6 cm PMMA blocks acquired with 40 mAs, 60 mAs, and 80 mAs. The method was evaluated in terms of average relative error of the standard deviation and NNPS, as defined by (21).

B. Human observer study

Inspired by Massoumzadeh *et al.* [31], a two-alternative forced-choice (2-AFC) study was conducted to confirm the equivalence in noise strength between simulated and real low-dose images in terms of human perception. The human observer study was conducted using images of a 3D anthropomorphic physical breast phantom, prototyped by CIRS, Inc. (Reston, VA) under license from the University of Pennsylvania [32]. The phantom consists of six slabs, each containing simulated anatomical structures manufactured using tissue mimicking materials, based upon a realization of the companion breast software phantom [33]. The physical phantom simulates a 450 ml breast, compressed to 5 cm, with 17% volumetric breast density (excluding the skin). Fig. 4 shows a photograph of the anthropomorphic breast phantom and an example of a DBT reconstructed central slice.

Real and simulated projections were reconstructed using a commercially available system (Briona Standard v4.0, Real Time Tomography, Villanova, PA). Reconstructed slices were evaluated using a RadiForce GS320 monitor (Eizo, Japan), with 3 MP resolution. The human observation study was conducted in a dark room appropriately prepared for this purpose, at the Hospital of the University of Pennsylvania. The readings were performed in one session per reader.

The observer study was organized as follows: five sets of projections were acquired using the anthropomorphic physical phantom at the radiographic factors given by the AEC (31 kV_p, tungsten target, aluminum filter and 60 mAs). The current-time product was then manually set to 30 mAs and the other five sets of projections were acquired. Using the standard-dose image (60 mAs), sets of projections were simulated at 30 mAs, 36 mAs, 42 mAs, 48 mAs, 54 mAs, and 59 mAs. Calibration projections, required by the simulation method, were acquired using the same radiographic factors as the AEC (31 kV_p, tungsten target, aluminum filter and 60 mAs), and a uniform block of PMMA with 4 cm. A collection of four ROIs at nine different depths was selected from each realization and each dose, resulting in one set of 180 real ROIs, and six sets of 180 simulated ROIs, one set at each current-time exposure mentioned above (30 mAs - 59 mAs).

Each observer was presented with 360 pairs of ROIs, extracted from the exact same location in the phantom. One image of the pair was a real acquisition at 30 mAs, while the other image was its simulated counterpart. Sixty simulated images were taken from the pool of 59 mAs, another sixty were taken from the pool of 54 mAs, and so on. The sequence of simulated images at different mAs was randomized prior to presenting them to the observer. The observer was asked to select the image that contained less noise. Observers were allowed to zoom and pan, the position of the observer in relation to the monitor was free, and no window or level tools were allowed.

Software developed for this work automatically recorded the observers' choices and time of decision. If the observer was incapable of perceiving any differences in noise levels, we expected that the simulated image would be chosen randomly 50% of the time. As the difference between noise levels increases, the percentage of correct selection should also increase, reaching 100% when differences are obvious. Ideally, we expect to achieve 50% of correct selection when the simulated exposure time matches the real exposure time (30 mAs in our experiment).

The 2-AFC study can also help to identify the just-noticeable difference (JND) noise for DBT images. In this context, the JND represents how much the current-time product has to be increased (or decreased) before human observers start to perceive a difference in noise levels. The JND point is defined at an accuracy of 75%, which is the midway between complete guessing (50%) and easily noticeable difference (100%) among simulated and real images. This information can also be used as a target for accuracy levels of noise simulation algorithms.

V. Results

The algorithm was validated using our MATLAB implementation. The method reported linear complexity, with approximately 2 Mpixel/s on a 3.40 GHz Intel Core i7-2600K CPU. Considering the size of the images simulated in this work (~3MP), the method simulates one DBT projection every 1.73 (± 0.09) seconds. The clinical unit used in this study acquires 15 projections per exam, thus a new full case is generated every 26 seconds.

A. Objective analysis

The standard deviation of the noise found at simulated and real acquisitions are presented in Fig. 5a and Fig. 5d.

Fig. 5a shows the local standard deviation of the noise at the central projection as a function of the distance to chest wall. Due to the flat-field calibration, the standard deviation of the noise increased as the distance to the chest wall increases, as expected [34]. Furthermore, the simulated values presented a good match visually with the real values. Fig. 5d shows the average error of the standard deviation of the simulated noise for different projections. Error bars represent the standard deviation of the error normalized by the square root of the number of samples. The average relative error was smaller than 2% for each projection angle.

The SNR calculated from simulated and real images are presented in Fig. 5b and Fig. 5e. Fig. 5b shows the local SNR at the central projection as a function of the distance to chest wall. As expected, when the noise standard deviation increased, the SNR decreased. Fig. 5e shows the average error of the SNR of the simulated and real images at different projections and doses. The error bars represent the standard deviation of the error normalized by the square root of the number of samples. The relative average error was smaller than 1% for all the projections.

The NNPS of the simulated and real acquisitions are presented in Fig. 5c and Fig. 5f. Fig. 5c shows the NNPS of the central projection for each simulated reduction. Fig. 5f shows the average error between the NNPS of the simulated and real images. Note that the proposed method was capable of accurately simulating the frequency-dependency of the noise. Error bars represent the standard deviation of the error normalized by the square root of the number of samples. The relative average error is smaller than 2.5% for all the projections.

Fig. 6 illustrates the importance of the spatial correlation considered in our noise model. The graph shows the NNPS calculated for a simulated image assuming that K_N is a dirac delta (i.e. without spatial correlation). The NNPS of a simulated image assuming spatial correlation is shown, estimating K_N using (16) and (19). Also shown is the NNPS of an actual acquisition at the simulated dose.

Dependency on calibration: To investigate the robustness of the proposed method to changes in the calibration image, the average relative error of the noise standard deviation and NNPS of the simulated images were analyzed at a range of beam qualities and PMMA thicknesses used for the calibration image; Fig. 7 shows the results. Fig. 7a shows the average relative error between the standard deviation of real and simulated noise. As expected, calibration images acquired at radiographic factors similar to the standard-dose image (60 mAs, 31 kVp, 4 cm) reported lower errors. Changes in mAs and thickness compensated each other, as seen at 80 mAs, 31 kVp, 6 cm. Fig. 7b shows the average relative error between the NNPS of real and simulated images. Again, the lowest error occurred when the calibration image was acquired at radiographic factors close to the standard-dose input image, and for a thickness similar to the patient's breast.

B. Human observer studies

The observer study allowed a subjective validation of the method. Fig. 8 (top row) shows a magnified ROI taken from raw projections of a real acquisition at 60 mAs (AEC), a simulated image at 30 mAs, and a real acquisition at 30 mAs. The difference in noise levels between 60 mAs and 30 mAs can be appreciated visually. Fig. 8 (bottom row) shows the residual noise for each ROI from Fig. 8 (top row). The residual noise was estimated by subtracting an approximation of the noise-free signal from one of the realizations. The noise-free approximation was obtained by averaging all five realizations of the phantom acquired at the same radiographic factors. Note that the differences in terms of the residual noise of the real 60 mAs and simulated 30 mAs (left and center) were easily noticeable, while simulated 30 mAs and real 30 mAs (center and right) were not discernible, indicating the good performance of the proposed method. Fig. 9 shows a magnified ROI taken from reconstructed slices acquired with 60 mAs, simulated 30 mAs starting from 60 mAs, and acquired with 30 mAs. Note that the differences in noise levels can be easily perceived when analyzing Figs. 9 (a) and (b). Meanwhile, no differences in noise levels can be seen in Figs. 9 (b) and (c), indicating the good performance of the simulation method.

TABLE I. Characteristics of the observers of the 2-AFC study

Observer	**1**	**2**	**3**	**4**	**5**	**6**
Experience (years)	20	5	9	1	5	16
Avg. reading time (s/pair)	12	8	12	6	8	11

A total of six medical physics specialists participated on the 2-AFC experiment to validate the noise levels in simulated images. Table I provides an overview of the observers' experience in the medical physics field, and the average reading time per image pair.

The frequency of correct selection – which we define as the selection of simulated images – and the average time of decision are shown in Fig. 10, as a function of the relative increase in the current time product.

The first important finding from Fig. 10a is the frequency of correct selection at which the current-time product of simulated and real images were a perfect match (0% increase). For an ideal test (infinite samples) and an ideal simulation method, the desired frequency would be 50%. Our experiment reported a frequency of 47% [38% 60%], where the brackets represent the 95% confidence interval (C.I.). As the 2-AFC task respects a binomial distribution, the theoretical 95% C.I. for random selection with the used number of trials for each observer (N=60) can be easily calculated, and is equal to [33% 63%]. Note that the correct selection rate of each observer falls within the theoretical interval.

Additionally, a hypothesis test was performed to investigate if the frequency of correct selection at 0% mAs increment is statistically different from random selection (50%). As the selection frequency follows a Binomial distribution, the arcsin transformation was first applied to the data. A Shapiro-Wilk test [35] confirmed the normality of the transformed distribution (p = 0.34). As the hypothesis cannot be rejected at a significance level of 95% (p = 0.84), the t-test suggests that the noise strength of simulated and real images are not discernably different by the human observers.

Fig. 10b shows an expected, but interesting trend in the

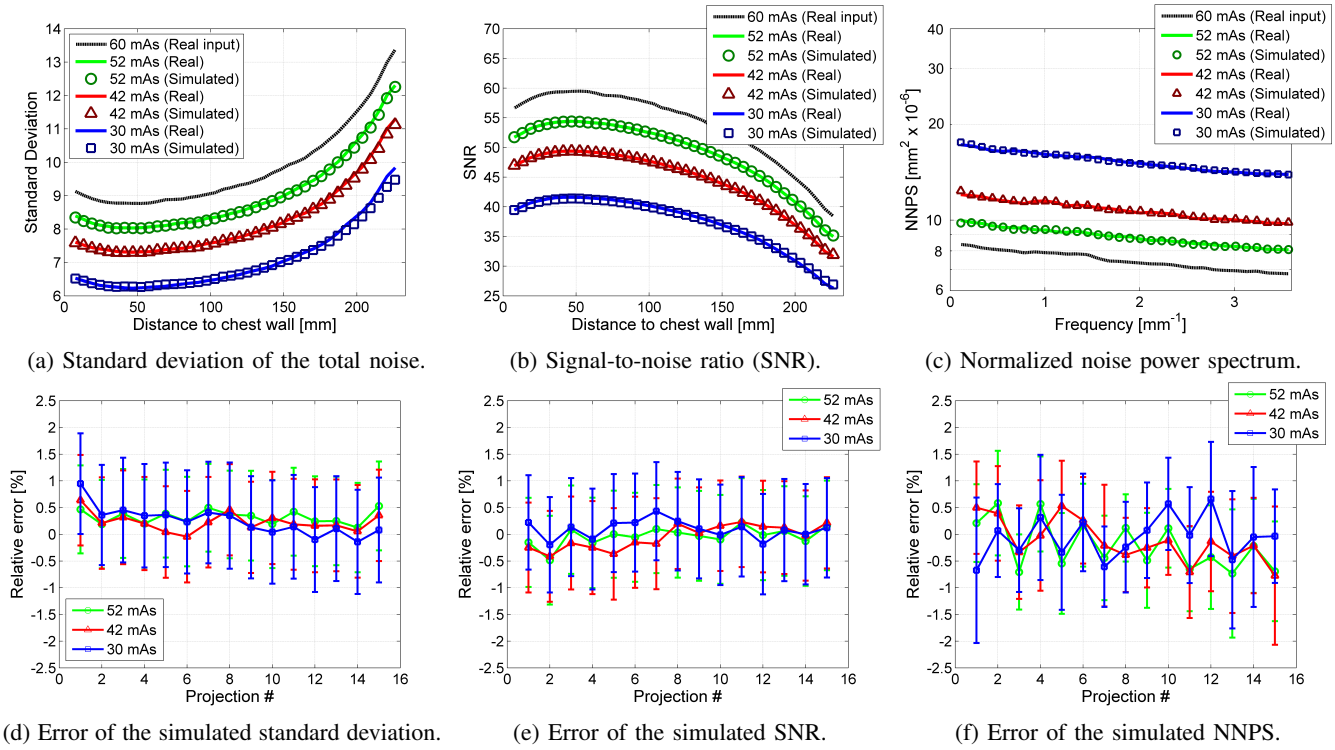

(a) Standard deviation of the total noise. (b) Signal-to-noise ratio (SNR). (c) Normalized noise power spectrum.

(d) Error of the simulated standard deviation. (e) Error of the simulated SNR. (f) Error of the simulated NNPS.

Fig. 5. Top row: objective metrics calculated at the central projection. Bottom row: average relative error between simulated and measured metrics. The bars represent the standardized errors.

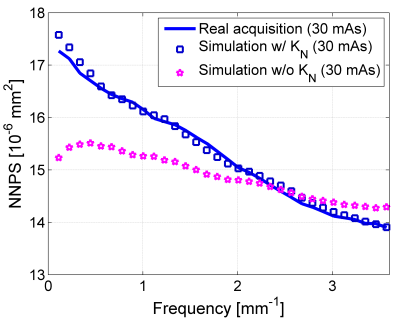

Fig. 6. Comparison of the simulated NNPS assuming no spatial correlation of the noise (w/o K_N), using the complete pipeline (w/ K_N), and the goal (real acquisition).

reading time. As the simulated and real images got more similar, the difficulty of choosing the correct image increased, causing the observer to spend more time trying to find the image containing less noise.

VI. Discussion and Conclusion

An accurate method for simulating dose reduction of DBT images was proposed in this work. It is a useful tool for studies of image quality, human perception and radiation dose when used in combination with DBT clinical images.

The work presented several innovations in relation to our previous methods [17]–[19]. The noise model accounts for flat-field corrections, electronic noise, and spatial correlation of the noise. Signal-dependent quantum noise was added though a novel operator developed for this purpose. Furthermore, the use of only one calibration image adds to the clinical practicality of the method.

Detailed descriptions of the method, materials and validation were provided. The work also presents experimental techniques, proposed by other authors, for estimating the parameters used in the simulation process. This is important as the parameter estimation plays a crucial role in the simulation method.

To ensure the clinical practicality of the method, the pixel crosstalk was modeled as a single convolution kernel K_N applied to both noise sources. This approximation can only be made under the assumption that the noise color, i.e. the slope of the NNPS curve, does not report relevant changes with dose. As a result, the spectrum of the simulated noise may report errors when simulating dose reduction on highly-correlated systems. Furthermore, the error of the NNPS may increase when the method is used to simulate very low doses.

Extensive validation was conducted to ensure the accuracy of the proposed method. Objective measurements were calculated on uniform images, where the estimation of signal and noise properties are straightforward. The standard deviation of the noise from simulated and real low-dose images were compared in Fig. 5a and Fig. 5d. The results provide evidence that the simulation method was capable of adding noise with the correct standard deviation, even considering the flat field correction, which is made evident by the increase in noise standard deviation for pixels far from the chest wall. No trend is observed when the projection angle of the acquisition is varied, indicating that the method performs well for oblique

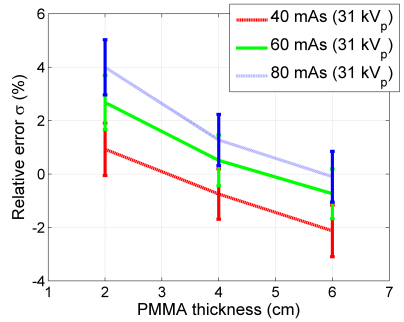

(a)

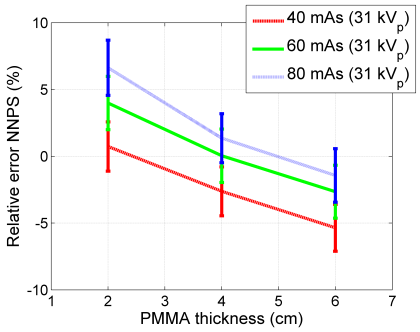

(b)

Fig. 7. Average relative error for a range of calibration images. (a) Error of the standard deviation of the simulated noise. (b) Error of the normalized noise power spectrum.

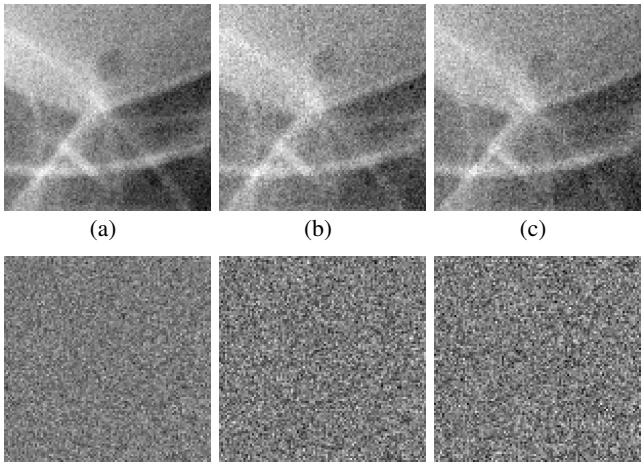

(a) (b) (c)

(d) (e) (f)

Fig. 8. Visual comparison between real and simulated projections. Raw magnified ROI (top row) and residual noise (bottom row) from acquisition with 60 mAs (a,d), simulation of 30 mAs starting from 60 mAs (b,e), acquisition with 30 mAs (c,f).

acquisition angles.

The second objective metric was the signal-to-noise ratio, presented in Fig 5b and Fig. 5e. As the noise standard deviation provides a good match, the SNR is an important indication that not only noise was simulated correctly, but also the scaling of the image signal. As expected, SNR drops farther from the chest wall, due to the higher standard deviation of the noise.

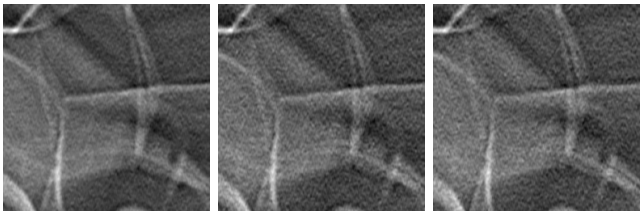

(a) (b) (c)

Fig. 9. Visual comparison between reconstructed slices from real and simulated projections. Magnified ROI from acquisition with 60 mAs (a), simulation of 30 mAs starting from 60 mAs (b), acquisition with 30 mAs (c).

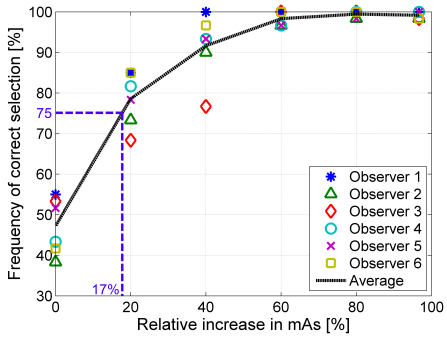

(a)

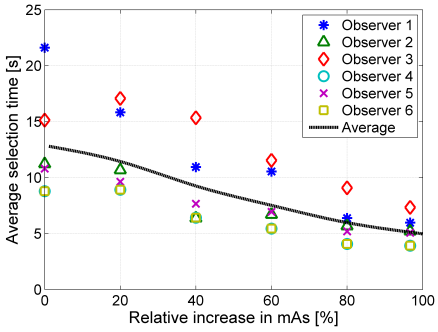

(b)

Fig. 10. Results from 2-AFC study. (a) Frequency of correct selection as a function of relative increment in mAs. (b) Time of decision as a function of relative increment in mAs.

The results presented in Fig. 5c and Fig. 5f shows that the spatial correlation, or pixel crosstalk, was simulated correctly in the low-dose images. The normalized noise power spectrum presented a good match with real low-dose acquisitions. Again, no trend can be seen as a function of the projection angle. Note that the correct simulation of the spatial correlation of the noise is crucial for the appropriate performance of readers when analysing simulated images. As spatially correlated noise presents some granularity, it represents an extra challenge to the image interpretation.

As the simulation method depends on a calibration image, we dedicated one section of this work to investigate how the use of non-ideal calibration images impacts the accuracy of the simulation method. The results indicate that it is possible to simulate dose reduction for a 4 cm case acquired at 60 mAs, using calibration images of phantoms from 2 cm to 6 cm

and with current-time product from 40 mAs to 80 mAs. The various combinations of these phantom thickness and current-time products yields errors lower than 6% in terms of standard deviation and 10% in terms of NNPS. We believe that these errors are acceptable, as previous work on CT [31], and photography [36] indicate that differences between 15% and 25% on the noise are not easily noticeable by human observers. Therefore, the proposed method is extremely flexible for clinical use, as a limited set of calibration images could be used to simulate dose reduction on an entire population.

The final validation was performed using a 3D anthropomorphic breast phantom and a 2-AFC observer study. As seen in Fig. 10, readers were not able to notice differences in the noise strength of simulated and real low-dose images, as the selection accuracy was close to random (50%). A Student's t-test was conducted and no statistical differences were found between the perception of noise strength from simulated and real images. Furthermore, Fig. 10 shows that the readers are good at detecting changes in noise levels - a relative increase of 20% in dose was enough to cause the correct selection rate to go from approx. 50% (guessing) to approx. 80%.

After the method was validated and the results indicated that the simulation was accurately performed, Fig. 10 can be interpreted to obtain a second important finding - the JND point. The JND value reported by this study was 17%, which falls within the range reported by others (15% - 25%) [31], [36]. While we no not claim that the dose for DBT examinations can be reduced without affecting the diagnostic outcome, in this study observers were not able to discern a 17% dose difference. The task of detection and lesion characterization were not considered in this work and would require a separate study.

In conclusion, we have proposed and validated a full pipeline capable of simulating dose reduction in DBT images. It considers both quantum and electronic noise and the spatial correlation of the pixels. We believe that the accuracy, along with the computational efficiency and flexibility of calibration make this method an attractive tool for clinical image-based simulations of dose reduction.

Appendix A. Spatially correlated signal-dependent noise

Let z_u denote the hypothetical signal measured by the detector if there were no crosstalk. The mean, variance, and PSD can be formalized as

$$\begin{aligned} \mathrm{E}\{z_u|y_u\} &= y_u + \tau_u, \\ \mathrm{var}\{z_u|y_u\} &= \lambda_u y_u + \sigma_u^2, \\ \Psi_{z_u} &= \|\lambda_u y_u + \sigma_u^2\|_1, \end{aligned}$$

where the noise corrupting z_u is spatially uncorrelated hence white (i.e. flat PSD). By modeling the effect of the detector crosstalk as the convolution of z_u with a kernel $K_u \geq 0$, we have

$$\begin{aligned} \mathrm{E}\{z_u \circledast K_u|y_u\} &= y_u \circledast K_u + \tau_u\|K_u\|_1, \\ \mathrm{var}\{z_u \circledast K_u|y_u\} &= \lambda_u y_u \circledast K_u^2 + \sigma_u^2\|K_u\|_2^2, \\ \Psi_{z_u \circledast K_u} &= |\mathcal{F}\{K_u\}|^2\|\lambda_u y_u + \sigma_u^2\|_1, \end{aligned} \tag{22}$$

Let the observations (1) originate from this process and set

$$\begin{aligned} y &= y_u \circledast K_u, \qquad \tau = \tau_u\|K_u\|_1, \\ z_{in} &= z_u \circledast K_u, \quad \lambda_{in} = \lambda_u \frac{\|K_u\|_2^2}{\|K_u\|_1}, \quad \sigma_E^2 = \sigma_u^2\|K_u\|_2^2. \end{aligned}$$

These substitutions trivially yield (1), (2), and (17), with $K_N = K_u\|K_u\|_2^{-1}$. We can then analyze the discrepancy between $\lambda_{in} y = \lambda_{in} y_u \circledast K_u$ from (3) and $\lambda_u y_u \circledast K_u^2 = \lambda_{in}\frac{\|K_u\|_1}{\|K_u\|_2^2} y_u \circledast K_u^2$ from (22). In particular, by taking the Maclaurin series of $y_u(t_0 - \cdot)$ at an arbitrary location t_0 and using 1D formalism [37],

$$\begin{aligned} [\lambda_{in} y_u \circledast K_u](t_0) &= \lambda_{in}\sum_t y_u(t_0 - t)\, K_u(t) = \\ &= \lambda_{in}\sum_t \sum_{k=0}^{+\infty} \frac{\partial^k y_u(t_0)\, t^k}{(-1)^k\, k!} K_u(t) = \\ &= \lambda_{in}\sum_{k=0}^{+\infty} \frac{\partial^k y_u(t_0)}{(-1)^k k!} \sum_t t^k K_u(t)\,, \end{aligned} \tag{23}$$

$$\begin{aligned} \left[\lambda_u y_u \circledast K_u^2\right](t_0) &= \lambda_{in}\frac{\|K_u\|_1}{\|K_u\|_2^2}\sum_t y_u(t_0 - t)\, K_u^2(t) = \\ &= \lambda_{in}\frac{\|K_u\|_1}{\|K_u\|_2^2}\sum_{k=0}^{+\infty} \frac{\partial^k y_u(t_0)}{(-1)^k k!} \sum_t t^k K_u^2(t)\,. \end{aligned} \tag{24}$$

Comparing the k-th summand in (23) with the corresponding summand in (24) we observe the following: the first summands (i.e. $k = 0$) coincide; if K_u is even symmetric, then the summands are zero for every odd k thanks to the odd symmetry of t^k. The above expressions generalize immediately to the 2D and higher-dimensional cases using the corresponding multi-index form of the Maclaurin series. Thus, the approximation

$$\mathrm{var}\{z_u \circledast K_u|y_u\} = \lambda_u y_u \circledast K_u^2 + \sigma_E^2 \approx \lambda_{in} y_u \circledast K_u + \sigma_E^2$$

is especially accurate when y_u is smooth, when K_u is symmetric, and in general when K_u has a small support, due to the properties of the Lagrange reminder. Hence, as $z_{in} = z_u \circledast K_u$ and $y = y_u \circledast K_u$, we can approximate

$$\mathrm{var}\{z_{in}|y_u\} \approx \lambda_{in} y + \sigma_E^2\,.$$

The conditioning upon y_u can be thus replaced by the pointwise conditioning upon y, leading to (3). Careful inspection of the plots of $\mathrm{var}\{z_{in}|y\}$ in Fig. 2 confirms the goodness of this approximation in the practice and its negligible impact to the accuracy of the final result, even for crosstalk kernels wider than that characteristic of the hardware in our experiments.

Appendix B. Operator Φ

In this appendix we demonstrate how the operator Φ was obtained, starting from a noisy input $z_\ell \geq 0$, such that:

$$z_\ell = y(\theta) + s(\theta)\,\xi_\theta, \qquad \xi_\theta \sim \Xi_\theta, \tag{25}$$

where $\theta \in \Theta \subseteq \mathbb{R}$ is the (unknown) parameter conditioning the system, $y(\theta) = \mathrm{E}\{z_\ell|\theta\} \geq 0$, $s(\theta) = \mathrm{std}\{z_\ell|\theta\} \geq 0$, ξ_θ, and Ξ_θ are, respectively, the conditional expectation, the conditional standard deviation, conditional standardized error, and the

standardized conditional distribution of z_ℓ. We represent Ξ_θ through its generalized probability density function p_θ,

$$\text{prob}\left(\xi_\theta \le \tau\right) = \int_{-\infty}^{\tau} p_\theta\left(\zeta\right) d\zeta. \tag{26}$$

Note that we can always identify θ with y, without loss of generality, as long as $y(\theta)$ is an invertible mapping of θ.

We consider a generic noise-injection operator Φ of the form

$$\Phi(z_\ell) = \frac{1}{c_1}\left(\frac{x^2}{4} - c_2 - \frac{\sigma_\text{A}^2}{4}\right),$$

where x is obtained by applying a root transformation f to z_ℓ followed by the addition of Gaussian noise,

$$x = f(z_\ell) + n = 2\sqrt{c_1 z_\ell + c_2} + \sigma_\text{A}\eta, \qquad \eta\left(\cdot\right) \sim \mathcal{N}(0,1)\,.$$

Throughout our analysis, we assume $c_1 \neq 0$, $c_2 \in \mathbb{R}$, and $c_1 z_\ell + c_2 \geq 0$ [1]. We are interested in the case $\sigma_\text{A} > 0$, for which $\Phi(z_\ell) \neq z_\ell$.

We treat $\left\{x^2 \middle| \theta\right\}$ as a mixture distribution with mixture components $\left\{x^2 \middle| \xi_\theta = \zeta\right\}$ and mixture density $p_\theta\left(\zeta\right)$, $\zeta \in \mathbb{R}$. According to this mixture model, we have

$$\text{E}\left\{\Phi\left[z_\ell\right]|\theta\right\} = \frac{1}{4c_1}\left[\int_{\mathbb{R}} m(\zeta)\, p_\theta(\zeta)\, d\zeta - 4c_2 - \sigma_\text{A}^2\right], \tag{27}$$

$$\begin{aligned}\text{var}\left\{\Phi\left[z_\ell\right]|\theta\right\} = \frac{1}{16c_1^2}\Bigg[&\int_{\mathbb{R}} \left(m^2(\zeta) + \varsigma^2(\zeta)\right) p_\theta(\zeta)\, d\zeta \\ &- \left(\int_{\mathbb{R}} m(\zeta)\, p_\theta(\zeta)\, d\zeta\right)^2\Bigg],\end{aligned} \tag{28}$$

where $m\left(\zeta\right)$ and $\varsigma^2\left(\zeta\right)$ are respectively the mean and variance of $\left\{x^2 \middle| \xi_\theta = \zeta\right\}$, and $\int_{\mathbb{R}} m(\zeta)\, p_\theta\left(\zeta\right) d\zeta = \text{E}\left\{x^2 \middle| \theta\right\}$.

For any given value of z_ℓ, the conditional distribution of x is a normal centered at $f(z_\ell)$:

$$\left\{x | z_\ell\right\} \sim \mathcal{N}\left(2\sqrt{c_1 z_\ell + c_2}, \sigma_\text{A}^2\right).$$

Hence,

$$\left\{x\sigma_\text{A}^{-1} \middle| z_\ell\right\} \sim \mathcal{N}\left(2\sigma_\text{A}^{-1}\sqrt{c_1 z_\ell + c_2}, 1\right).$$

Therefore, for any given value of z_ℓ, $x^2\sigma_\text{A}^{-2}$ follows a non-central χ^2 distribution with 1 degree of freedom and non-centrality parameter $\mu^2 = \text{E}^2\{x\sigma_\text{A}^{-1}|z_\ell\}$. The conditional expectation and variance are thus

$$\begin{aligned}\text{E}\left\{x^2\sigma_\text{A}^{-2} \middle| z_\ell\right\} &= 1 + \mu^2 = 1 + 4\left(c_1 z_\ell + c_2\right)\sigma_\text{A}^{-2}, \\ \text{var}\left\{x^2\sigma_\text{A}^{-2} \middle| z_\ell\right\} &= 2 + 4\mu^2 = 2 + 16\left(c_1 z_\ell + c_2\right)\sigma_\text{A}^{-2}.\end{aligned}$$

Consequently,

$$\text{E}\left\{x^2 \middle| \xi_\theta = \zeta\right\} = m(\zeta) = \sigma_\text{A}^2 + 4\left[c_1\left(y(\theta) + s(\theta)\,\zeta\right) + c_2\right], \tag{29}$$

$$\text{var}\left\{x^2 \middle| \xi_\theta = \zeta\right\} = \varsigma^2(\zeta) = 2\sigma_\text{A}^4 + 16\sigma_\text{A}^2\left[c_1\left(y(\theta) + s(\theta)\,\zeta\right) + c_2\right]. \tag{30}$$

[1] In practice, negative samples can be replaced by 0, defining $f(z_\ell) = 2\sqrt{\max\left\{0, c_1 z_\ell + c_2\right\}}$. This non-negative clipping may lead to some imprecision if the proportion of negative samples is significant, e.g., if $\text{prob}\left(\xi_\theta \le \frac{-1}{s(\theta)}\left(\frac{c_2}{c_1} + y\left(\theta\right)\right)\right) > 0.05$.

Substituting (29) into (27) yields

$$\text{E}\{\Phi(z_\ell)|\theta\} = y(\theta) + s(\theta)\int_{\mathbb{R}} \zeta\, p_\theta(\zeta)\, d\zeta = y(\theta) = \text{E}\{z_\ell|\theta\}, \tag{31}$$

where the last identity follows from ξ_θ being a standardized error, thus $\int_{\mathbb{R}} \zeta\, p_\theta(\zeta)\, d\zeta = \text{E}\{\xi_\theta|\theta\} = 0$. Eq. (31) means that Φ operates an *exact unbiased injection* of noise. Note that this is valid regardless of the particular choice of c_1, c_2, and σ_A.

Next, we substitute (29) and (30) into (28). Simplifications lead to

$$\text{var}\left\{\Phi\left[z_\ell\right]|\theta\right\} = s^2(\theta) + \frac{\sigma_\text{A}^4}{8c_1^2} + \frac{\sigma_\text{A}^2 c_2}{c_1^2} + \frac{\sigma_\text{A}^2 y(\theta)}{c_1}, \tag{32}$$

where, in order to deduce $\int_{\mathbb{R}} \zeta^2 p_\theta(\zeta)\, d\zeta = \text{var}\left\{\xi_\theta|\theta\right\} = 1$, we again leverage the fact that ξ_θ is a standardized error.

It is important to note that (31) and (32) are valid for arbitrary conditional standard deviation $s(\theta)$ and standardized conditional distribution Ξ_θ of z_ℓ.

For the specific case of a z_ℓ as in (7), we have an affine variance $s^2(\theta) = \lambda_\text{in} y(\theta) + \sigma_\text{E}^2$, with $\lambda_\text{in} > 0$ and $\sigma_\text{E}^2 \in \mathbb{R}$; thus

$$\text{var}\left\{\Phi\left[z_\ell\right]|\theta\right\} = \left(\lambda_\text{in} + \frac{\sigma_\text{A}^2}{c_1}\right) y(\theta) + \sigma_\text{E}^2 + \frac{\sigma_\text{A}^4}{8c_1^2} + \frac{\sigma_\text{A}^2 c_2}{c_1^2}. \tag{33}$$

Therefore, to obtain a signal-dependent target variance where only the linear portion of the variance function is modified, we have

$$\text{var}\left\{\Phi\left[z_\ell\right]|\theta\right\} = \lambda_\text{out} y(\theta) + \sigma_\text{E}^2, \tag{34}$$

with $\lambda_\text{out} > \lambda_\text{in}$, it suffices to set

$$c_1 = \frac{\sigma_\text{A}^2}{\lambda_\text{out} - \lambda_\text{in}}, \quad c_2 = -\frac{\sigma_\text{A}^2}{8}. \tag{35}$$

In particular, for the observations (1)–(3) and goals described by (4) and (5), we have $\lambda_\text{out} = \lambda_\text{in}/\gamma$, $\sigma_\text{A} = \sqrt{(1/\gamma) - 1}$.

The application described in this work has observations with a signal intensity offset τ. The variable z_ℓ considers that such offset has been removed, as done in Section III-B. Furthermore, all the above derivations involve pointwise operations and thus they hold also when the noise η is spatially correlated (i.e. frequency-dependent); only its variance and Gaussian distribution matter. To simulate the spatial correlation due to detector crosstalk, η is obtained by convolving white Gaussian noise against a kernel K_N (20). Neither the variance nor the Gaussianity of η are affected by this operation.

Acknowledgment

The authors would like to thank Real Time Tomography for providing the reconstruction software, Ms. Kristen Lau for her support during the acquisition of images, and the team of medical physicists who volunteered for participating in the 2-AFC experiment. ADAM is a member of the scientific advisory board, and a shareholder of RTT.

REFERENCES

[1] C. I. Lee, M. Cevik, O. Alagoz, B. L. Sprague, A. N. Tosteson, D. L. Miglioretti, K. Kerlikowske, N. K. Stout, J. G. Jarvik, S. D. Ramsey *et al.*, "Comparative effectiveness of combined digital mammography and tomosynthesis screening for women with dense breasts," *Radiology*, vol. 274, no. 3, pp. 772–780, 2014.

[2] F. J. Gilbert, L. Tucker, M. G. Gillan, P. Willsher, J. Cooke, K. A. Duncan, M. J. Michell, H. M. Dobson, Y. Y. Lim, T. Suaris *et al.*, "Accuracy of digital breast tomosynthesis for depicting breast cancer subgroups in a UK retrospective reading study (TOMMY trial)," *Radiology*, vol. 277, no. 3, pp. 697–706, 2015.

[3] R. G. Roth, A. D. Maidment, S. P. Weinstein, S. O. Roth, and E. F. Conant, "Digital breast tomosynthesis: lessons learned from early clinical implementation," *Radiographics*, vol. 34, no. 4, pp. E89–E102, 2014.

[4] S. S. J. Feng and I. Sechopoulos, "Clinical digital breast tomosynthesis system: dosimetric characterization," *Radiology*, vol. 263, no. 1, pp. 35–42, 2012.

[5] T. Svahn, N. Houssami, I. Sechopoulos, and S. Mattsson, "Review of radiation dose estimates in digital breast tomosynthesis relative to those in two-view full-field digital mammography," *The Breast*, vol. 24, no. 2, pp. 93–99, 2015.

[6] International Atomic Energy Agency, "Appendix II: Medical exposure," in *International Basic Safety Standards for Protection against Ionizing Radiation and for the Safety of Radiation Sources*, 1996, pp. 45–56.

[7] I. Sechopoulos and C. Ghetti, "Optimization of the acquisition geometry in digital tomosynthesis of the breast," *Med. Phys.*, vol. 36, no. 4, pp. 1199–1207, 2009.

[8] H. Machida, T. Yuhara, T. Mori, E. Ueno, Y. Moribe, and J. M. Sabol, "Optimizing parameters for flat-panel detector digital tomosynthesis," *RadioGraphics*, vol. 30, no. 2, pp. 549–562, 2010, pMID: 20228334. [Online]. Available: http://dx.doi.org/10.1148/rg.302095097

[9] L. R. Borges, P. R. Bakic, A. Foi, A. D. A. Maidment, and M. A. C. Vieira, "Pipeline for effective denoising of digital mammography and digital breast tomosynthesis," in *Proc. SPIE Medical Imaging 2017: Physics of Medical Imaging*, vol. 10132, no. 1013206, 2017. [Online]. Available: http://dx.doi.org/10.1117/12.2255058

[10] T. Wu, R. H. Moore, E. A. Rafferty, and D. B. Kopans, "A comparison of reconstruction algorithms for breast tomosynthesis," *Med. Phys.*, vol. 31, no. 9, pp. 2636–2647, 2004.

[11] E. Y. Sidky, X. Pan, I. S. Reiser, R. M. Nishikawa, R. H. Moore, and D. B. Kopans, "Enhanced imaging of microcalcifications in digital breast tomosynthesis through improved image-reconstruction algorithms," *Med. Phys.*, vol. 36, no. 11, pp. 4920–4932, 2009.

[12] A. Svalkvist and M. Båth, "Simulation of dose reduction in tomosynthesis," *Med. Phys.*, vol. 37, no. 1, pp. 258–269, 2010. [Online]. Available: http://dx.doi.org/10.1118/1.3273064

[13] A. Mackenzie, D. R. Dance, A. Workman, M. Yip, K. Wells, and K. C. Young, "Conversion of mammographic images to appear with the noise and sharpness characteristics of a different detector and x-ray system," *Med. Phys.*, vol. 39, no. 5, pp. 2721–2734, 2012.

[14] A. Mackenzie, D. R. Dance, O. Diaz, and K. C. Young, "Image simulation and a model of noise power spectra across a range of mammographic beam qualities," *Med. Phys.*, vol. 41, no. 12, p. 121901, 2014.

[15] E. Samei, R. S. Saunders Jr, J. A. Baker, and D. M. Delong, "Digital mammography: Effects of reduced radiation dose on diagnostic performance 1," *Radiology*, vol. 243, no. 2, pp. 396–404, 2007.

[16] R. S. Saunders, J. A. Baker, D. M. Delong, J. P. Johnson, and E. Samei, "Does image quality matter? Impact of resolution and noise on mammographic task performance," *Med. Phys.*, vol. 34, no. 10, pp. 3971–3981, 2007.

[17] L. R. Borges, M. A. da Costa Vieira, and A. Foi, "Unbiased injection of signal-dependent noise in variance-stabilized range," *IEEE Signal Proc. Let.*, vol. 23, no. 10, pp. 1494–1498, Oct 2016.

[18] L. R. Borges, H. C. de Oliveira, P. F. Nunes, P. R. Bakic, A. D. Maidment, and M. A. Vieira, "Method for simulating dose reduction in digital mammography using the Anscombe transformation," *Med. Phys.*, vol. 43, no. 6, pp. 2704–2714, 2016.

[19] L. R. Borges, I. Guerrero, P. R. Bakic, A. D. Maidment, H. Schiabel, and M. A. Vieira, "Simulation of dose reduction in digital breast tomosynthesis," in *International Workshop on Digital Mammography*. Springer, 2016, pp. 343–350.

[20] I. Sechopoulos, "A review of breast tomosynthesis. Part I. The image acquisition process," *Med. Phys.*, vol. 40, no. 1, p. 014301, 2013.

[21] S. Vedantham, A. Karellas, G. R. Vijayaraghavan, and D. B. Kopans, "Digital breast tomosynthesis: state of the art," *Radiology*, vol. 277, no. 3, pp. 663–684, 2015.

[22] N. H. Marshall, "Calculation of quantitative image quality parameters," NHSBSP Equipment Report 0902, 2009.

[23] I. Cunningham, "Applied linear-system theory," in *Handbook of Medical Imaging: Physics and Psychophysics*, R. Van Metter, J. Beutel, and H. Kundel, Eds. SPIE, 2000, pp. 79–155.

[24] J. Lee and K. Hoppel, "Noise modeling and estimation of remotely-sensed images," in *1989 IEEE Int. Geoscience and Remote Sensing Symposium (IGARSS'89)*, vol. 2, 1989, pp. 1005–1008.

[25] A. Foi, M. Trimeche, V. Katkovnik, and K. Egiazarian, "Practical Poissonian-Gaussian noise modeling and fitting for single-image raw-data," *IEEE T. Image Process.*, vol. 17, no. 10, pp. 1737–1754, 2008.

[26] N. Acito, M. Diani, and G. Corsini, "Signal-dependent noise modeling and model parameter estimation in hyperspectral images," *IEEE T Geosci. Remote*, vol. 49, no. 8, pp. 2957–2971, 2011.

[27] A. Foi. (2016) Signal-dependent noise modeling, estimation, and removal for digital sensors. [Online]. Available: www.cs.tut.fi/~foi/sensornoise

[28] F. J. Anscombe, "The transformation of Poisson, binomial and negative-binomial data," *Biometrika*, vol. 35, no. 3/4, pp. 246–254, 1948.

[29] K. Young and J. Oduko, "Technical evaluation of the Hologic Selenia full-field digital mammography system with a tungsten tube," *NHS Cancer Screening Programmes*, 2008.

[30] J. T. Dobbins III, "Image quality metrics for digital systems," in *Handbook of Medical Imaging: Physics and Psychophysics*, R. Van Metter, J. Beutel, and H. Kundel, Eds. SPIE, 2000, pp. 79–155.

[31] P. Massoumzadeh, S. Don, C. F. Hildebolt, K. T. Bae, and B. R. Whiting, "Validation of CT dose-reduction simulation," *Med. Phys.*, vol. 36, no. 1, pp. 174–189, 2009.

[32] L. Cockmartin, P. R. Bakic, H. Bosmans, A. D. Maidment, H. Gall, M. Zerhouni, and N. W. Marshall, "Power spectrum analysis of an anthropomorphic breast phantom compared to patient data in 2D digital mammography and breast tomosynthesis," in *International Workshop on Digital Mammography*. Springer, 2014, pp. 423–429.

[33] D. D. Pokrajac, A. D. Maidment, and P. R. Bakic, "Optimized generation of high resolution breast anthropomorphic software phantoms," *Med. Phys.*, vol. 39, no. 4, pp. 2290–2302, 2012.

[34] M. Yaffe, "Digital mammography," in *Handbook of Medical Imaging: Physics and Psychophysics*, R. Van Metter, J. Beutel, and H. Kundel, Eds. SPIE, 2000, pp. 329–372.

[35] S. S. Shapiro and M. B. Wilk, "An analysis of variance test for normality (complete samples)," *Biometrika*, vol. 52, no. 3/4, pp. 591–611, 1965.

[36] D. Zwick and D. L. Brothers, "RMS granularity: Determination of just noticeable differences," *Photogr. Sci. Eng.*, vol. 19, no. 4, pp. 235–238, 1975.

[37] L. Azzari and A. Foi, "Variance stabilization in Poisson image deblurring," in *Proc. 2017 IEEE Int. Sym. Biomedical Imaging (ISBI)*, Melbourne, Australia, 2017.